Research Article

Preparation of micro-mesoporous carbon from seawater-impregnated sawdust by low temperature one-step CO_2 activation for adsorption of oxytetracycline

Renwen Ma[1] · Yuhui Ma[1] · Yan Gao[2] · Junrui Cao[1]

Received: 14 November 2019 / Accepted: 3 January 2020 / Published online: 9 January 2020

Abstract
Porous carbons (PCs) were prepared from seawater (SW)-impregnated sawdust (SD) by CO_2 activation at 700 °C. The preparation process was investigated on-line by thermogravimetric analyzer coupled with FTIR (TG-FTIR). PCs were characterized by N_2-adsorption/desorption and Fourier transform infrared spectroscopy. The adsorption abilities of PCs for oxytetracycline (OTC) were compared and the adsorption isotherms of OTC on the optimum sample were studied. Results showed that SW impregnation led to the release of more CO from SD at 700 °C, indicating a higher degree of CO_2 activation, thus a 81% higher BET surface area (S_{BET}) can be achieved under the same activation condition. Mesopore volume of PC increased from 0.089 to 0.301 $cm^3\ g^{-1}$ with the activation time increasing from 5 to 60 min. PC obtained after 60-min activation with a S_{BET} of 490 $m^2\ g^{-1}$ and an average pore diameter of 3.78 nm had the highest adsorption ability for OTC. Its adsorption equilibrium data for OTC followed Langmuir model with a maximum monolayer adsorption capacity up to 100 mg g^{-1}.

Keywords Porous carbon · CO_2 activation · Seawater · TG-FTIR · Adsorption

1 Introduction

Porous carbon (PC) material is most commonly used as an adsorbent because of its high surface area and large-scale production possibility [1–3]. Activated carbon and biochar are two typical kinds of PC materials, and they have been widely applied in the adsorption removal of nutrients [4], heavy metals [5, 6], antibiotics [7], dyes [8] and so on. Pore structure is one of the most important features of PC considering its applications in adsorption processes involving organic compounds in liquid phase [9]. Although the development of micropores smaller than 2 nm can lead to high surface area, they restrict mass transfer and reduce pore accessibility to large adsorbates [10]. For example, the high molecular weight organics contained in wastewater may cause micropore blockage and reduce the adsorption capacity of PC, while mesopore (2 nm < diameter < 50 nm) is the main transfer artery for large molecules, higher mesoporosity may benefit for the adsorbates transfer from liquid solutions to solid adsorbents [11–14]. Thus, recently, much attention has been paid to the preparation of PC with a reasonable distribution over the diameter ranges of both micropores and mesopores.

Activation has been proved as a powerful way of enhancing porosity of PC and improving its performance as an adsorbent [15–17]. Chemical activation is a single-stage process that includes impregnation of raw materials using activating agents such as KOH, K_2CO_3, NaOH, $ZnCl_2$, H_3PO_4 and H_2SO_4 prior to heat treatment in an inert atmosphere, and these activating agents can improve the pore

✉ Yuhui Ma, myhbiomass@163.com | [1]The Institute of Seawater Desalination and Multipurpose Utilization (ISDMU), Ministry of Natural Resources of the People's Republic of China, Tianjin 300192, China. [2]School of Pharmaceutical Science and Technology, Tianjin University, Tianjin 300072, China.

distribution and increase the surface area [18, 19]. The activation temperature depends on the type of activating agents, for example, 400–500 °C for H_3PO_4 and 500–700 °C for $ZnCl_2$ [20]. The use of chemicals results in risks of equipment corrosion and secondary environmental pollution during disposal [21, 22], and these factors have led to a greater number of studies on physical activation that occurs through oxidation with an oxidizing gas (CO_2 or water vapor). However, physical activation always takes place at higher temperatures (800–1000 °C), leading to a huge consumption of energy [21, 23]. Thus, exploring a new way to carry out physical activation at lower temperatures for shorter periods of time will be a desirable feature in the field of activated carbon industry.

Traditionally, physical activation consists of two main stages: carbonization of raw materials under an inert atmosphere, followed by the heat treatment under the oxidizing gas atmosphere such as water vapor, CO_2 and air at an elevated temperature ranging between 800 and 1000 °C [18]. Unlike two-step procedure, in one-step procedure, the temperature is ramped up from room temperature to the required activation temperature, and both carbonization and activation steps are carried out simultaneously in the presence of oxidizing agents. One-step activation is preferable because of the reduced production costs in terms of time and energy [24]. For example, Yang et al. reported that activated carbon with high BET surface area of 1667 $m^2\ g^{-1}$ can be directly prepared from coconut shell by one-step CO_2 activation at 900 °C for 140 min [25]; Gonçalves et al. found that compared with two-step CO_2 activation, one-step activation resulted in a higher BET surface area of the activated carbon using bagasse/molasses pellet as the raw material [26].

Recently, CO_2 has become the preferred oxidizing gas because it facilitates control of the activation process due to its lower reactivity than water vapor at high temperature [27–29]. Moreover, it contributes to both water-saving and offering a potential solution for the alleviation of greenhouse gas emitted from industrial facilities [30, 31]. The essence of CO_2 activation is the partial gasification of the carbonaceous materials with CO_2, resulting in the removal of carbon atoms and simultaneously producing pores [25]. There have already been some published papers related with CO_2 gasification of biomass chars in the presence of alkali and alkaline earth metals (AAEMs) as catalysts, which could change electron-cloud distribution of the surface atoms, promoting chars to participate in the gasification reaction and inhibiting the graphitization or condensation of char [32, 33]. For example, Perander et al. found that the gasification rate of the spruce wood char increased linearly with an increase in the concentration of Ca or K [34]. Lv et al. reported that AAEM species existing in biomass increased the char reactivity, resulting in the decrease of initial gasification temperature and the increase of the peak gasification value [35]. It was found by Lahijani et al. that activation energy of the gasification reaction between pistachio nut shell char and CO_2 can be reduced by 53 kJ/mol by adding 5 wt% $NaNO_3$ [30]. However, these previous studies focused on the gasification behaviors of chars, such as carbon conversion rate, gas yield, gasification reactivity and kinetics, there was no information about the pore structure of the solid porous char. Sadhwani et al. took the surface area of char into consideration when studying the AAEMs-catalyzed CO_2 gasification kinetics of pine char, the emphasis of their study was the validation of the random pore model (RPM) to predict the gasification process, and there was a lack of the data about the evolution of pore volume and pore size distribution [31]. Overall, there has been limited published work aimed at the preparation of PC via AAEMs catalyzed CO_2 activation.

It is a general knowledge that seawater (SW) is naturally high in Na, Mg, Ca and K salts [36, 37], thus SW could be a cost-effective source of AAEMs for catalyzing CO_2 activation. However, there has been no report on this topic. In the present study, sawdust (SD), a common kind of low-cost biomass material, was impregnated with SW and then used for the preparation of micro-mesoporous carbon. The main contributions of the work are as follows: (1) the effects of SW impregnation on thermal decomposition and activation behaviors of SD under CO_2 were clarified using thermogravimetric analyzer coupled with a Fourier transform infrared spectrometer (TG-FTIR); (2) the evolution of the porous structure of the final products was summarized based on N_2-adsorption/desorption data, and the surface functional groups were characterized using FTIR; (3) the relationship between the pore structure and the adsorption capacity of the product to oxytetracycline (OTC), a most common antibiotic detected in aquatic environments, was established, and the adsorption equilibrium isotherms of OTC by the optimum product were determined. In order to more fully understand the work, the graphical abstract is shown in Fig. 1.

2 Experimental

2.1 Materials

Poplar SD was dried at 100 °C for 24 h, then ground and sieved into particle sizes of 80 to 120 mesh prior to use. Seawater (SW) was collected from South China Sea and filtered through 0.22 μm membranes to eliminate dirt before use. The concentrations of sodium (10.8 g L^{-1}), potassium (399 mg L^{-1}), magnesium (1.31 g L^{-1}), calcium (421 mg L^{-1}) in SW were determined by an inductively coupled plasma

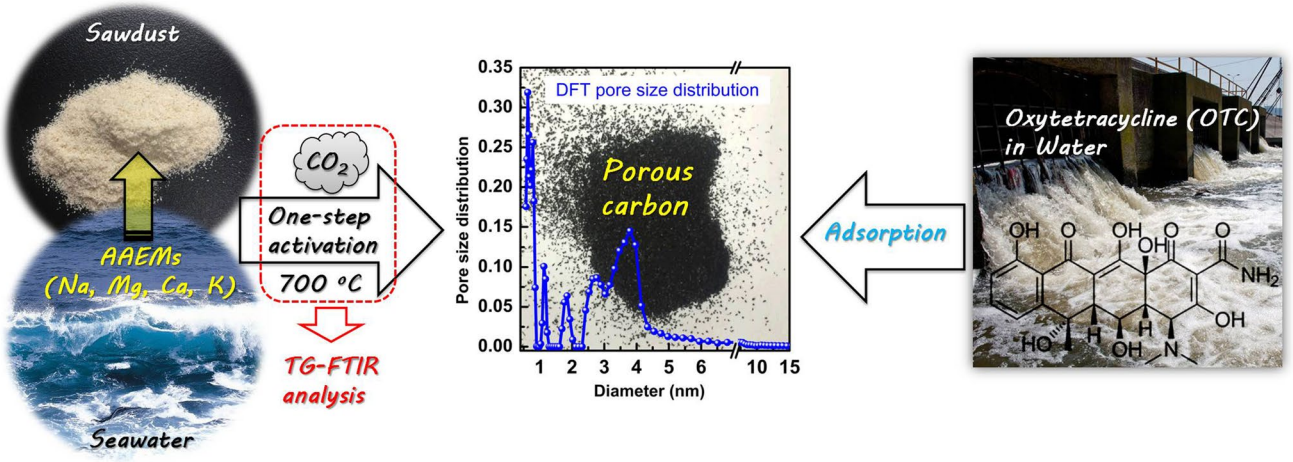

Fig. 1 Graphical abstract of the study

mass spectrometry (ICP-MS) (iCAP Q, Thermo Scientific, USA).

2.2 Preparation of porous carbons

SD was mixed with SW under a ratio of 100 g:1L, then the mixture was agitated in a shaker at 180 rpm for 12 h. After impregnation, the mixture was vacuum filtered and the solid was dried in an oven at 100 °C for 24 h (labeled as SW–SD). SW–SD was heated at a temperature increasing with a heating rate of 5 °C min^{-1} to a final temperature of 700 °C under pure CO_2 atmosphere with the flow rate of 200 mL min^{-1} in a tube furnace (CTF12/65/550, Carbolite, Great Britain). The final temperature was maintained for 5, 20, 40 and 60 min, respectively. The products were cooled under CO_2 flow, then washed with 0.1 M HCl solution and distilled water to a neutral pH, followed by drying at 105 °C for 8 h. The final products were denoted $PC_{SW/CO2/700/05}$, $PC_{SW/CO2/700/20}$, $PC_{SW/CO2/700/40}$ and $PC_{SW/CO2/700/60}$. The yield of product was calculated from the following equation:

$$Yield(\%) = \frac{M_{Carbon}}{M_{SD}} \times 100 \quad (1)$$

where M_{Carbon} is the mass of the product, and M_{SD} is the mass of SD used as raw material. For comparison, porous carbons were also obtained from SD without SW impregnation under N_2 and CO_2 atmosphere at 700 °C for 20 min according to the same process, and the products were labeled as $PC_{N2/700/20}$ and $PC_{CO2/700/20}$, respectively.

2.3 Characterization of porous carbon

Pore characteristics of the samples were analyzed with N_2-adsorption/desorption using a gas adsorption apparatus (Autosorb-iQ, Quantachrome Instruments, USA) at − 196 °C, and BET surface area (S_{BET}) and the successive pore size distribution from micropores to mesopores were calculated using Brunauer–Emmett–Teller (BET) method and density function theory (DFT), respectively. The total pore volume (V_{Total}) was estimated from liquid volume of N_2 adsorbed at the saturation of relative pressure. Horvath–Kawazo (HK) and Barret–Joyner–Halenda (BJH) method were used to deduce the micropore volume (V_{Micro}) and the mesopore volume (V_{Meso}), repectively. The average pore diameter (D_{Avg}) was calculated as $D_{Avg} = 4V_{Total}/S_{BET}$. The surface functional groups were investigated by FTIR (TENSOR II, Bruker, Germany).

2.4 Adsorption study

2.4.1 Comparison of adsorption capacity

Aqueous solution of OTC was prepared with concentration of 100 mg L^{-1}. 10 mg of $PC_{SW/CO2/700/05}$, $PC_{SW/CO2/700/20}$, $PC_{SW/CO2/700/40}$ and $PC_{SW/CO2/700/60}$ were added to each aqueous solution (20 mL) contained in 50 mL Erlenmeyer flasks. Adsorption equilibrium was reached after the Erlenmeyer flasks agitated in a shaker at 180 rpm and room temperature for 24 h. The suspensions were filtered by 0.45 µm membrane filters and the filtrates were diluted to a suitable concentration. The concentrations of OTC in the diluted filtrates were determined using a UV–Vis spectrophotometer (DR5000, HACH, USA) at the maximum wavelengths (λ) of 268 nm. OTC removal efficiency [*RE* (%)] was calculated from the following equation:

$$RE(\%) = \frac{C_0 - C_e}{C_0} \times 100 \quad (2)$$

where C_0 and C_e (mg L^{-1}) are the initial and equilibrium liquid-phase concentrations of OTC.

2.4.2 Adsorption equilibrium isotherms

The optimal PC sample (10 mg) selected based on Sect. 2.4.1 and aqueous solution (20 mL) of OTC contained in 50 mL Erlenmeyer flasks were agitated in a shaker at 180 rpm and room temperature for 24 h. The initial concentrations of OTC ranged from 20 to 120 mg L^1. The concentrations of OTC in the suspensions were determined as described in Sect. 2.4.1. OTC uptake per unit mass of porous carbon at equilibrium [q_e (mg g^1)] was calculated from the following equation:

$$q_e = \frac{C_0 - C_e}{W} V \quad (3)$$

where C_0 and C_e (mg L^{-1}) are the initial and equilibrium liquid-phase concentrations of OTC. V (L) is the volume of the solution and W (g) is the mass of porous carbon used. The equilibrium data were modelled using Langmuir, Freundlich and Temkin isotherm models and the model equations are shown in Table 1 [38].

2.5 TG-FTIR analysis

Thermal behaviors and gaseous products obtained during the thermal treatments of SD and SW-SD was studied using a TG-FTIR instrument that consists of a simultaneous thermal analyzer (STA 2500 Regulus, NETZSCH, Germany) and a Fourier transform infrared spectrometer (TENSOR II, Bruker, Germany). For comparison, SD was also pre-treated with deionized water according to the same process of SW impregnation, and the product was denoted as W-SD. SD, SW-SD and W-SD (about 13 mg) were heated from 35 °C to 1000 °C at CO_2 flowing rate of 70 mL min^{-1} and the heating rate of 20 °C min^{-1}. The volatiles released during heating were detected by FTIR, and the spectra was recorded at 4000–600 cm^{-1} with a resolution of 4 cm^{-1}. To minimize secondary reactions, both the transfer pipe and the gas cell were heated at a constant temperature of 200 °C.

3 Results and discussion

3.1 TG-FTIR study

3.1.1 Thermal behavior

Figure 2 shows the TG and derivative thermogravimetry (DTG) curves of SD, SW-SD and W-SD. The characteristic parameters obtained from the TG and DTG curves such as the temperature ranges of the weight losses, the maximum weight loss rates (R_{max}) of the weight loss stages, and the corresponding temperature (T_{max}) are shown in Table 2. For SD, the weight loss below 200 °C indicated the loss of moisture, and the major weight loss appeared within the temperature of 220–410 °C, with the maximum weight loss rate peak at 365 °C, indicating the decomposition of hemicellulose and cellulose. The weight loss rate became quite slow above 410 °C because the violent cracking of organic compounds finished at this stage. Instead, the polycondensation of carbonaceous matters in the residue became the primary reaction, leading to the release of small molecules at a slow rate. The final weight loss stage above 840 °C indicated the gasification reaction between the solid char derived from SD and CO_2 atmosphere.

There were also four stages in the weight loss process of SW-SD, but its weight loss rate became obviously higher than that of SD above 320 °C, and the maximum weight loss rate peak of SW-SD appeared at 344 °C. The major weight loss process of SW-SD finished at 370 °C, indicating that AAEMs in SW were helpful for the decomposition of the bio-polymers (mianly hemicellulose, cellulose and lignin) in SD at low temperatures. Besides, the residue rate of SW-SD was higher than that of SD between 390 and 845 °C, suggesting that the AAEMs also benefited the formation of solid char. The above results were similar to those in a previous study [39]. The maximum weight loss

Table 1 Linear and non-linear forms of Langmuir, Freundlich, and Temkin isotherm models

Model	Non-linear form	Linear form	Plot
Langmuir	$q_e = \frac{q_m K_L C_e}{1+K_L C_e}$	$\frac{C_e}{q_e} = \frac{C_e}{q_m} + \frac{1}{K_L q_m}$	$\frac{C_e}{q_e}$ versus C_e
Freundlich	$q_e = K_F C_e^{1/n}$	$\log q_e = \log K_F + \frac{1}{n} \log C_e$	$\log q_e$ versus $\log C_e$
Temkin	$q_e = B_T \ln (A_T C_e)$	$q_e = \frac{RT}{b} \ln A_T + \frac{RT}{b} \ln C_e$	q_e versus $\ln C_e$

q_m (mg g^{-1}) is the maximum monolayer adsorption capacity of the sorbent, K_L (L mg^{-1}) is the Langmuir constants related to the free energy or net enthalpy of adsorption. K_F (mg g^{-1}) (L $mg^{-1})^{1/n}$ is Freundlich adsorption constant, indicating the relative adsorption capacity of the adsorbent, n represents the adsorption intensity, and values of $n > 1$ indicate favorable nature of adsorption. $B_T = RT/b$, with b (J mol^{-1}), A_T (L g^{-1}), R (8.314 J mol^{-1} K^{-1}) and T (K) are the Temkin constant related to heat of sorption, equilibrium binding constant, gas constant and absolute temperature, respectively

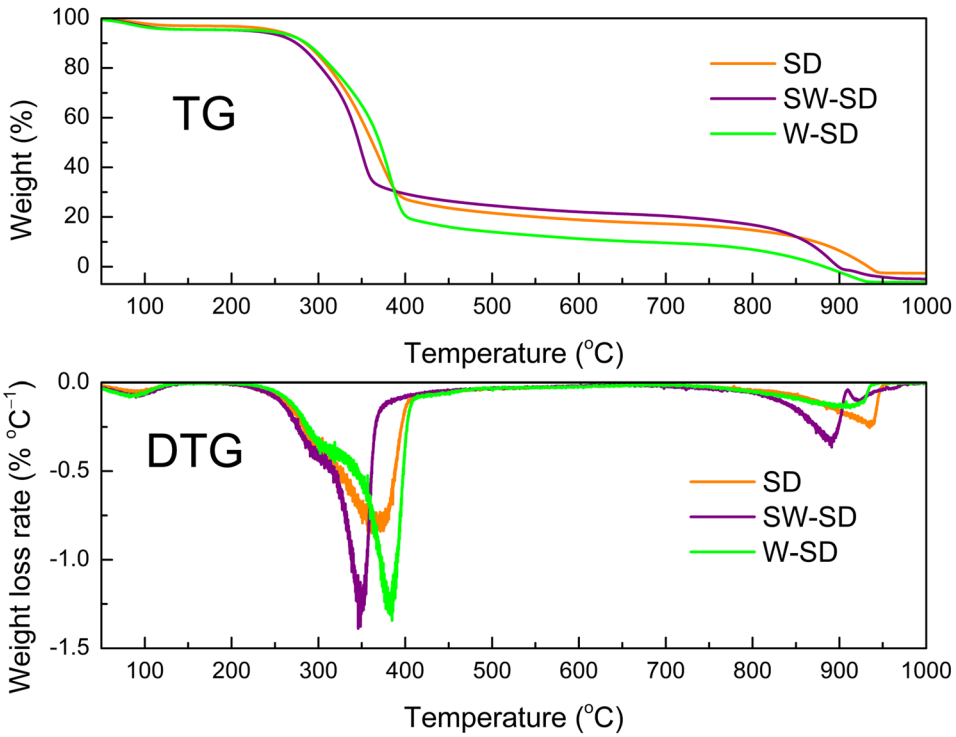

Fig. 2 TG and DTG curves of SD, SW-SD and W-SD.

Table 2 Characteristic parameters obtained from TG and DTG data for samples

Sample	Temperature range (°C)	T_{max} (°C)	R_{max} (%°C^{-1})	Comment
SD	50–140	90	0.06	Water evaporation
	220–410	365	0.84	Pyrolysis of organics
	410–820	–	–	Polycondensation
	820–950	935	0.24	CO_2 gasification of char
SW-SD	50–140	90	0.09	Water evaporation
	220–370	344	1.38	Pyrolysis of organics
	370–800	–	–	Polycondensation
	800–910	890	0.35	CO_2 gasification of char
W-SD	50–130	85	0.08	Water evaporation
	230–415	385	1.31	Pyrolysis of organics
	415–800	–	–	Polycondensation
	800–935	910	0.14	CO_2 gasification of char

rate temperature of the final weight loss stage of SW-SD was 890 °C, which was 45 °C lower than that of SD, proving that the AAEMs in SW had catalytic effects on the gasification of SD char by CO_2.

The thermal decomposition process of W-SD can also be divided into four stages, which were evaporation, pyrolysis, polycondensation and gasification. The temperature of the maximum weight loss rate of W-SD was 385 °C, which was 20 °C higher than that of SD, indicating that the thermal stability of SD was enhanced by water-washing. Moreover, W-SD had a lower residue rate than SD above 390 °C. In addition, R_{max} of CO_2 gasification of W-SD char was only 0.14% °C^{-1}, which was the lowest among these of the three samples. It is interesting to note that the above mentioned changing trends were just opposite to these of SW-SD. The results were due to the fact that the removal of the intrinsic water-soluble AAEMs from SD by water washing reduced the catalytic effect on promoting thermal decomposition, char formation and CO_2 gasification [35, 40].

3.1.2 Analysis of gaseous products

The volatiles evolved from the thermal decomposition of SD, SW-SD and W-SD were analyzed by FTIR in real time. As can be seen from Fig. 3a, the Gram-Schmidt curves shows the variation of the yields of the volatile compounds with temperature. SD curve had two peaks centered at 348 and 932 °C while SW-SD curve had two peaks centered at 343 and 886 °C. For W-SD, the two peaks appeared at 377 and 905 °C. The Gram-Schmidt peaks of the samples matched well with their DTG peaks. 3D (absorbance-wavenumber-temperature) spectra of the volatiles generated from SD, SW-SD and W-SD can be seen from Fig. 3b, c, respectively. When the temperature is fixed, absorbance at different wavenumber can be obtained to study the volatile

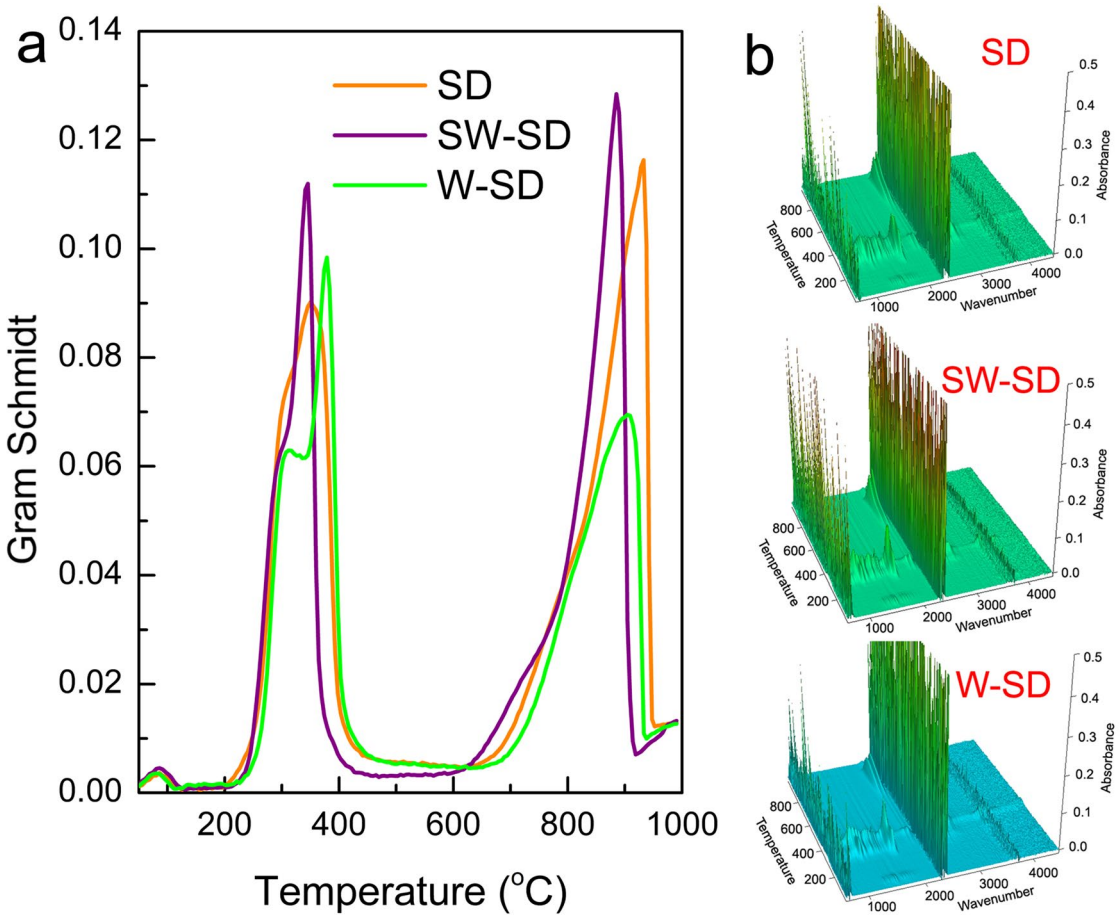

Fig. 3 **a** Gram–Schmidt curve of SD, SW-SD and W-SD at the heating rate of 20 °C min^{-1}, **b** 3-D infrared spectra of gaseous products from SD, SW-SD and W-SD.

components released at this moment. Figure 4 shows the FTIR spectra at the peak temperatures for SD and SW-SD. The gaseous products composed of a variety of molecules were evolved from SD due to the thermal cracking of the bio-polymers (mainly cellulose) at 348 °C. The peaks centered at 3575 and 1515 cm^{-1} represented –OH bond stretching vibrations in H_2O. The band between 3015 and 2650 cm^{-1} indicated the stretching vibration of C–H in aliphatic hydrocarbons. The presence of CO led to the presence of two subtle peaks at 2174 and 2102 cm^{-1}. The most remarkable absorbance peak at 1772 cm^{-1} belonged to C=O stretching in carboxylic acids, ketones and aldehydes. The peak at 1394 cm^{-1} can be assigned to the stretching vibration of C–H, indicating the release of aliphatic hydrocarbons. The peaks at 1177 and 1110 cm^{-1} can be attributed to the stretching vibration of C–O–C in ethers. With the temperature increased to 932 °C, only two sharp adjacent peaks attributed to CO can be observed. This was because almost all the organics in SD were decomposed at this high temperature, and the violent gasification of SD char by CO_2 led to the generation of CO and the formation of pores in char. SW-SD and W-SD spectra at 343 and 377 °C show that the gaseous components were not altered due to SW impregnation and water washing, but the relative contents of these components were changed. CO was also the only gaseous product evolved from SW-SD and W-SD at 886 and 905 °C, indicating the occurrence of gasification of SW-SD and W-SD char.

Since CO was the only product generated during CO_2 activation, the evolution history of CO absorbance as a function of temperature are presented in Fig. 5a. CO produced at the low temperatures was caused by the breakage of ether bonds and C=O bonds during the pyrolysis of SD, SW-SD and W-SD [41], while a large amount of CO released above 650 °C indicated the occurrence of activation reactions. Figure 5b shows the variation of the difference between the absorbances of CO released from SW-SD ($Abs_{SW\text{-}SD}$), W-SD ($Abs_{W\text{-}SD}$) and SD (Abs_{SD}) with temperature. As can be seen, SW impregnation led to two positive peaks at 700 and 890 °C, indicating that more CO was released from SW-SD than from SD at these two temperatures, and a larger amount of CO represented a

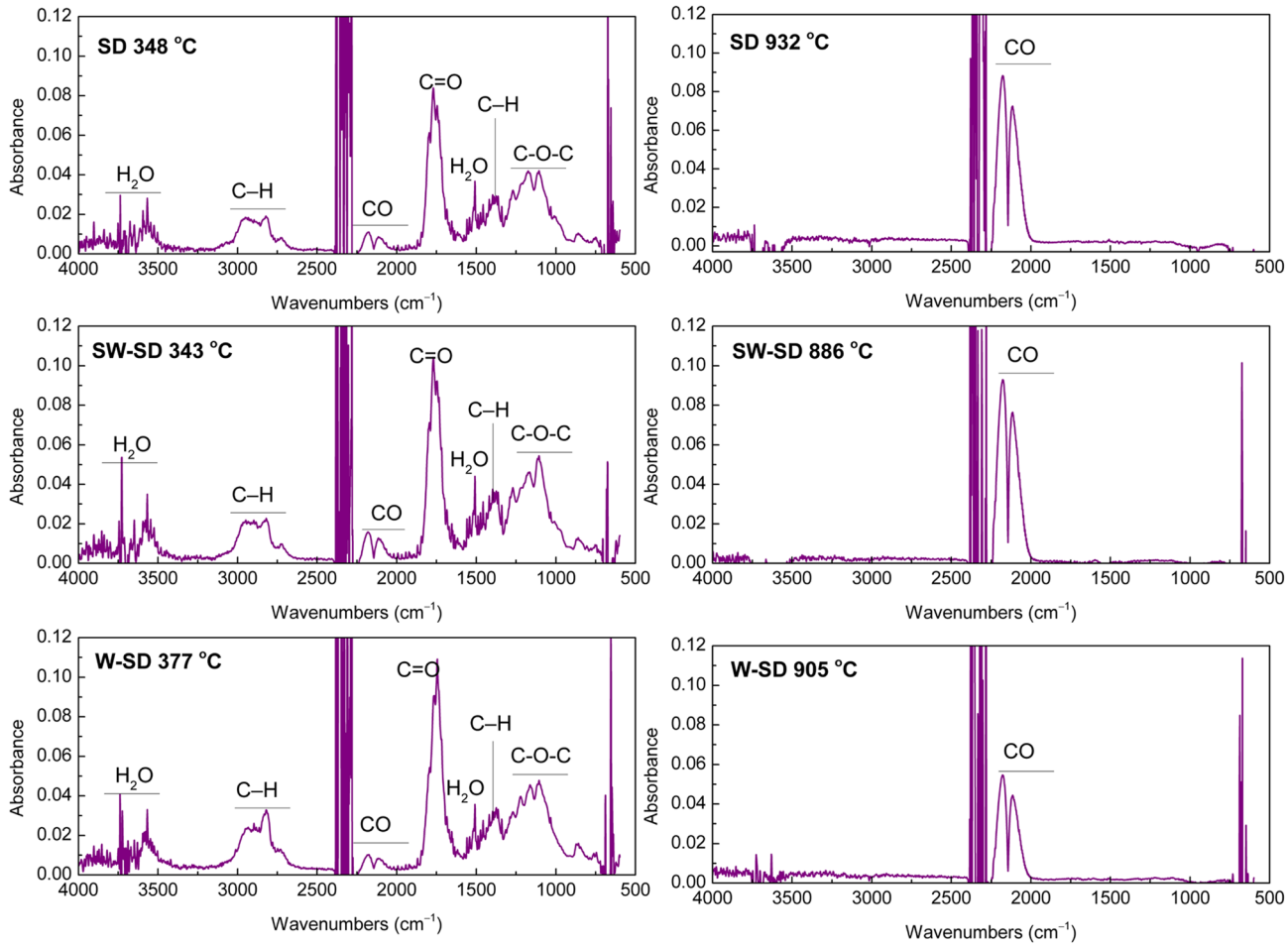

Fig. 4 FTIR spectra for gaseous products from SD, SW-SD and W-SD corresponding to typical temperatures.

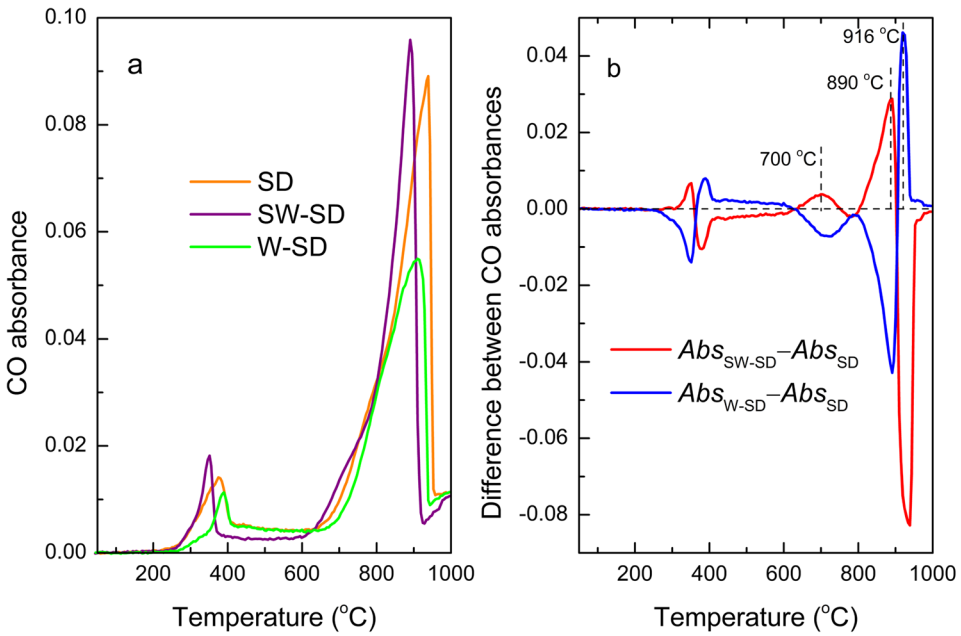

Fig. 5 **a** Evolution curves of CO from SD, SW-SD and W-SD at the heating rate of 20 °C min^{-1}, **b** variation of the difference between the absorbances of CO released from SD, SW-SD and W-SD with temperature.

higher degree of CO_2 activation. In contrast, less CO was produced from W-SD than from SD during the CO_2 activation stage until the temperature reached as high as 905 °C. Thus, SW-SD was more suitable than SD and W-SD for the preparation of PC via CO_2 activation, and 700 °C was selected as the final activation temperature in the follow-up experiments in the aim of energy-saving. Besides, this temperature was much lower than the commonly used CO_2 activation temperatures (800–1000 °C).

3.2 Characterization of porous carbons

N_2-adsorption/desorption isotherms of the PCs are shown in Fig. 6. The adsorption isotherms of the samples show the remarkable nitrogen uptakes in the low pressure region ($P/P_0 \le 0.05$), standing for the presence of micropores (diameter ≤ 2 nm). The adsorbed volumes at high relative pressures after the initial filling suggested the presence of mesopores (2 nm < diameter < 50 nm). The isotherms of $PC_{N2/700/200}$ and $PC_{SW/CO2/700/05}$ exhibited relatively sharp knees and they appeared to be of type I according to the IUPAC classification, reflecting the predominance of microporosity. The isotherms of $PC_{CO2/700/20}$, $PC_{SW/CO2/700/20}$ $PC_{SW/CO2/700/40}$ and $PC_{SW/CO2/700/60}$ displayed type IV isotherms that had more rounded knees pointing to a widening of microporosity that even extended to mesoporosity. Moreover, the distinct hysteresis loops can be observed from the isotherms of $PC_{SW/CO2/700/20}$ $PC_{SW/CO2/700/40}$ and $PC_{SW/CO2/700/60}$, indicating the existence of abundant mesopores with an interconnected multistage channel structure.

Pore characteristic parameters of the samples measured by the N_2-adsorption/desorption isotherms are shown in Table 3. $PC_{CO2/700/20}$ had a lower S_{BET} than $PC_{N2/700/20}$ because CO_2 etching effect led to the expansion of micropores into mesopores. $PC_{SW/CO2/700/05}$ had a S_{BET} of 572 $m^2\ g^{-1}$, and it consisted mainly of micropores, indicating that a highly microporous carbon can be prepared from SW-SD in only 5 min. This was because the gasification reaction can be significantly promoted by the AAEMs

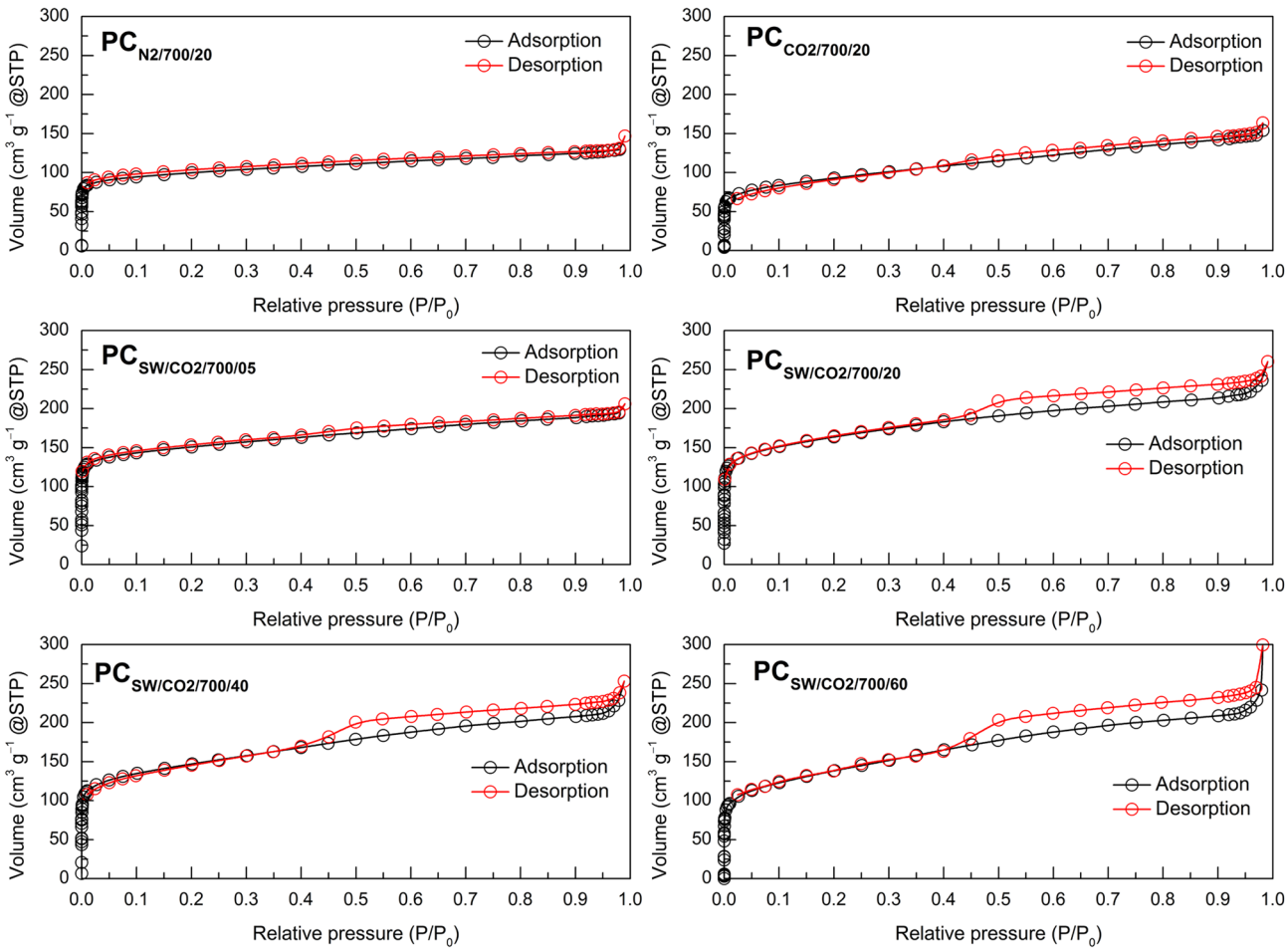

Fig. 6 N2-adsorption/desorption curves of porous carbons.

Table 3 Pore characteristics of porous carbons

Sample	S_{BET} (m^2/g)	V_{Total} (cm^3/g)	V_{Micro} (cm^3/g)	V_{Meso} (cm^3/g)	D_{Avg} (nm)	*Yield* (%)
$PC_{N2/700/20}$	376	0.227	0.150	0.074	2.41	19.42
$PC_{CO2/700/20}$	331	0.238	0.137	0.109	2.87	15.84
$PC_{SW/CO2/700/05}$	572	0.319	0.228	0.089	2.23	20.03
$PC_{SW/CO2/700/20}$	600	0.402	0.245	0.171	2.68	16.48
$PC_{SW/CO2/700/40}$	532	0.392	0.219	0.198	2.94	16.43
$PC_{SW/CO2/700/60}$	490	0.463	0.203	0.301	3.78	16.30

contained in SW. The increase of activation time from 5 to 20 min led to the formation of both more micro- and mesopores, thus $PC_{SW/CO2/700/20}$ had the highest S_{BET} of 600 $m^2\ g^{-1}$ among the samples. Note that S_{BET} of $PC_{SW/CO2/700/20}$ was 1.8 times higher than that of $PC_{CO2/700/20}$, proving that AAEMs in SW played an important role in promoting pore formation during CO_2 activation. With the activation time increasing to 40 and 60 min, V_{Micro} decreased while V_{Meso} increased because CO_2 etching of original micropore walls led to pore widening and formation of mesopores. It is worth noting although $PC_{SW/CO2/700/60}$ had a relatively low S_{BET} of 490 $m^2\ g^{-1}$, it had the highest proportion of mesopore (65%), and its D_{avg} reached as large as 3.78 nm. Thus it can be said that $PC_{SW/CO2/700/60}$ was a typical micro-mesoporous carbon. The comparison of the pore characteristics of $PC_{SW/CO2/700/60}$ with some micro-mesoporous carbons is listed in Table 4.

To find out the detail effects of CO_2 activation and SW impregnation on porous structures of the products, DFT pore size distribution curves of $PC_{N2/700/20}$, $PC_{CO2/700/20}$, and $PC_{SW/CO2/700/20}$ were compared. As can be seen from Fig. 7, $PC_{N2/700/20}$ had a strong peak at 0.54 nm and a distribution between 1.20 and 1.50 nm. The porous structure of $PC_{N2/700/20}$ was determined by the natural properties of the raw material SD because no reactive gas was introduced during the heating process. Compared with $PC_{N2/700/20}$, $PC_{CO2/700/20}$ had a much weaker peak at 0.63 nm, and a weaker distribution between 1.14 and 1.48 nm. However, the distribution of $PC_{CO2/700/20}$ curve within the diameter ranges of 0.64–0.90, 1.48–2.03, and especially 2.25–4.50 nm were stronger than $PC_{N2/700/20}$. The results indicated that reaction between CO_2 and char led to micropore widening and formation of more mesopores. $PC_{SW/CO2/700/20}$ had obviously more micropores than $PC_{CO2/700/20}$ within the range of diameter smaller than 0.61 nm, and it also an even stronger distribution than $PC_{N2/700/20}$ between 1.14 and 1.48 nm. Moreover, $PC_{SW/CO2/700/20}$ contained more mesopores with diameter of 3.50–4.24 nm than $PC_{CO2/700/20}$. The above results proved that CO_2 activation of SD led to the expansion of original micropores into mesopores compared with carbonization of SD under inert atmosphere, but pre-impregnation of SD with SW was apparently beneficial to the formation of both more micro- and mesopores during CO_2 activation.

To determine the influences of activation time on the porous structures of the products, DFT pore size distribution curves of $PC_{SW/CO2/700/05}$, $PC_{SW/CO2/700/20}$, $PC_{SW/CO2/700/40}$ and $PC_{SW/CO2/700/60}$ are compared in Fig. 8. $PC_{SW/CO2/700/20}$ had stronger distribution than $PC_{SW/CO2/700/05}$ within the whole diameter range, except the peak at 0.51 nm obviously decreased. Therefore, more micro- and mesopores were created in the carbon matrix with the activation time increasing from 5 to 20 min. The strongest peak shifted from 0.51 to 0.58 nm when the activation time increased to 40 min. In addition, the distribution between 1.16 and 1.50 nm decreased while more pores were formed with the diameter between 2.32 and 4.40 nm. Activation time extended to 60 min led to stronger distribution within the ranges of 0.65–0.90, 1.81–2.02 and especially 2.32–4.40 nm. However, the maximum peak value of $PC_{SW/CO2/700/60}$ curve appeared at 0.63 nm and it was much lower than that of the other three curves.

To characterize the surface groups on the porous carbons, FTIR spectra of $PC_{SW/CO2/700/05}$, $PC_{SW/CO2/700/20}$,

Table 4 Comparison of the pore characteristics of $PC_{SW/CO2/700/60}$ with some micro-mesoporous carbons

Precursor	S_{BET} (m^2/g)	V_{Total} (cm^3/g)	V_{Micro} (cm^3/g)	V_{Meso} (cm^3/g)	D_{Avg} (nm)	Refs.
Semi-coke	121				6.49	[1]
Peanut hulls	600	0.427		0.188	2.85	[44]
Water fern	641	0.460	0.196		2.87	[45]
Chitosan flakes	318	0.255			3.20	[46]
Lemna minor	531	1.0	0.078	0.922	7.5	[47]
Palm oil cooking waste	497	0.389			3.13	[48]
Sawdust	490	0.463	0.203	0.301	3.78	This study

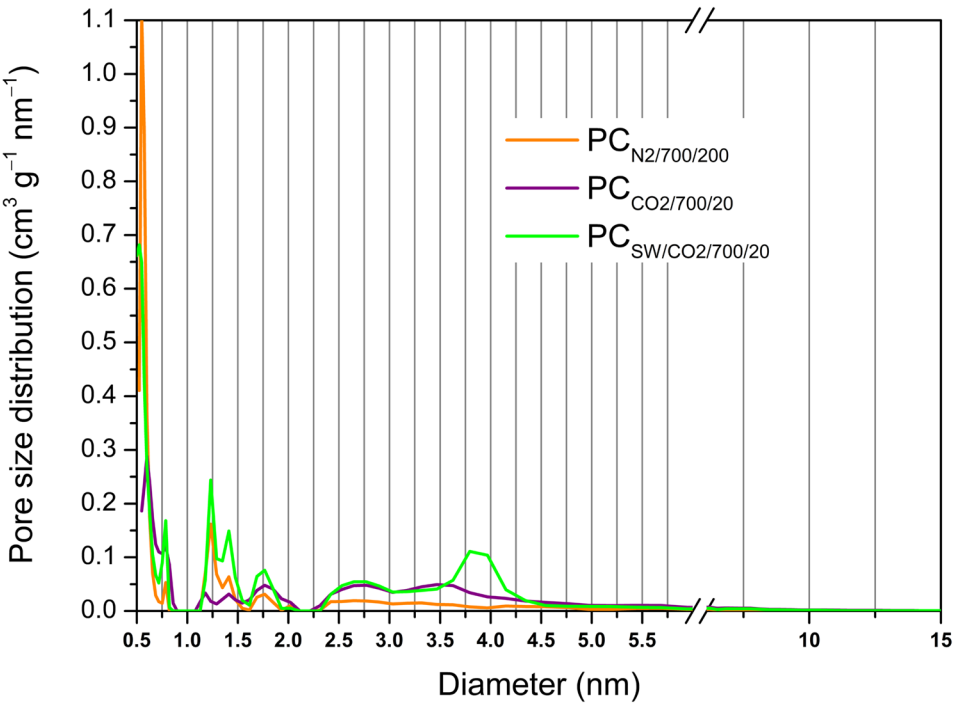

Fig. 7 DFT pore size distribution curves of $PC_{N2/700/20}$, $PC_{CO2/700/20}$, and $PC_{SW/CO2/700/20}$.

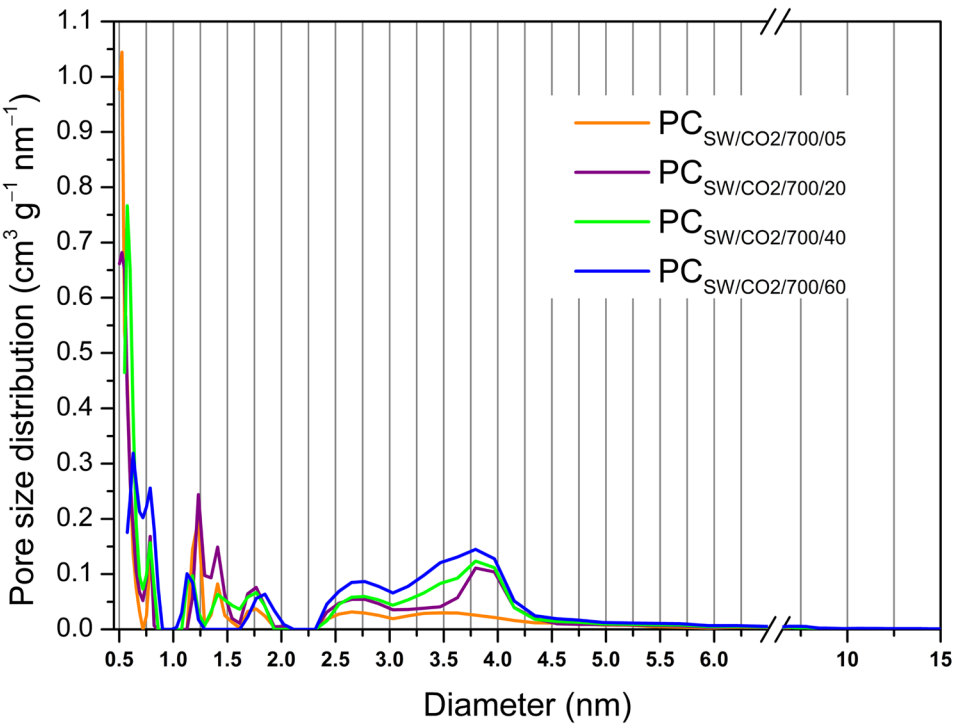

Fig. 8 DFT pore size distribution curves of $PC_{SW/CO2/700/05}$, $PC_{SW/CO2/700/20}$, $PC_{SW/CO2/700/40}$, and $PC_{SW/CO2/700/60}$.

$PC_{SW/CO2/700/40}$ and $PC_{SW/CO2/700/60}$ were recorded (Fig. 9). As can be seen, activation time had no significant influence on the position and intensity of the adsorption peaks. The strong peak at 3448 cm^{-1} was caused by the presence of O–H and bands around 2928 and 2853 cm^{-1} indicated the presence of C–H stretching in aliphatic hydrocarbons. The peak at 1628 cm^{-1} can be attributed to the stretching vibration of C=O conjugated to the aromatic rings. The peak at 1070 cm^{-1} demonstrated the presence of C–O–C in ethers [42].

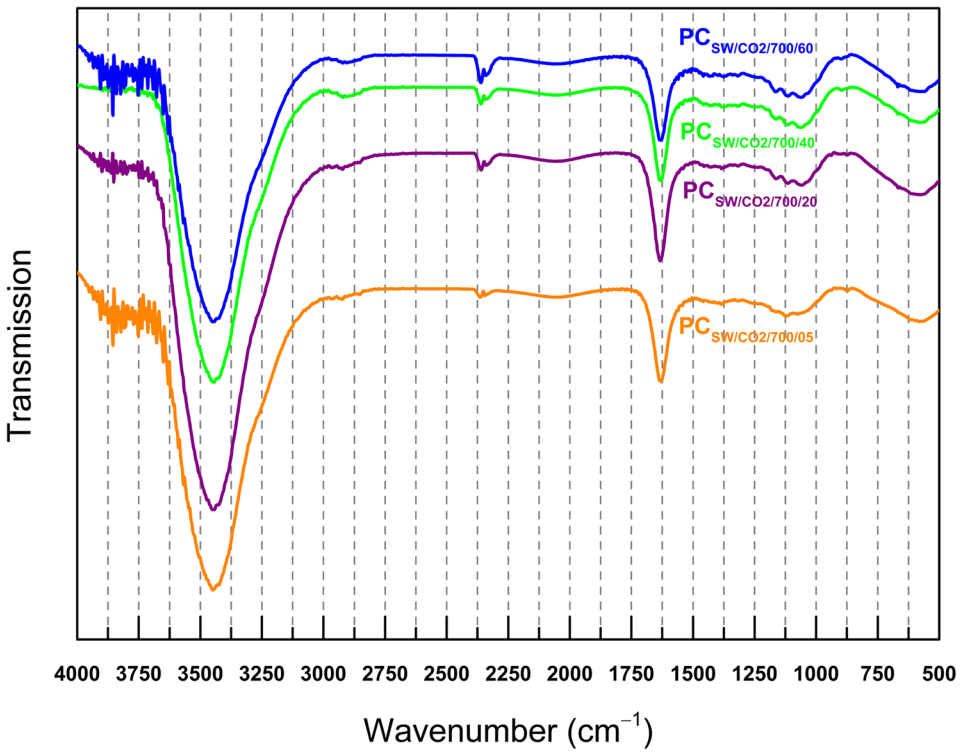

Fig. 9 FTIR spectra of $PC_{SW/CO2/700/05}$, $PC_{SW/CO2/700/20}$, $PC_{SW/CO2/700/40}$, and $PC_{SW/CO2/700/60}$.

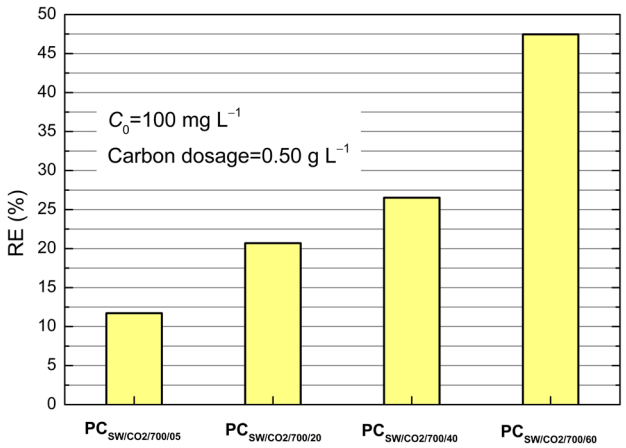

Figure 10 Removal efficiencies of $PC_{SW/CO2/700/05}$, $PC_{SW/CO2/700/20}$, $PC_{SW/CO2/700/40}$ and $PC_{SW/CO2/700/60}$ for OTC.

3.3 Adsorption study

The removal efficiencies of $PC_{SW/CO2/700/05}$, $PC_{SW/CO2/700/20}$, $PC_{SW/CO2/700/40}$ and $PC_{SW/CO2/700/60}$ for OTC are shown in Fig. 10. Interestingly, although $PC_{SW/CO2/700/60}$ had lower surface area compared with other samples, it had the highest removal efficiency of 47.64% under the same experimental condition. Figure 11a, b show that the q_e values of the samples had positive correlation with their V_{Meso} and D_{Avg}, respectively. Moreover, the higher corresponding correlation coefficient R^2 of 0.9942 suggested that q_e had a better linear relationship with D_{Avg} than with V_{Meso}. Thus, D_{Avg} can be possibly used as an index for the prediction of adsorption capacity of a PC sample for OTC.

$PC_{SW/CO2/700/60}$ had a much better adsorption performance than other samples, thus the adsorption isotherm study was focused on $PC_{SW/CO2/700/60}$. The adsorption isotherm is shown in Fig. 12a, as can be seen, the increase in initial concentration of OTC resulted in the increase of adsorption equilibrium, this was because the initial concentration provided a driving force for OTC transferred from the aqueous phase to the surface of $PC_{SW/CO2/700/60}$. Figure 12b–d shows the linear fitting of adsorption equilibrium data by Langmuir, Freundlich and Temkin isotherm models, and the best fitting model was determined by the highest R^2 value. R^2 values and the isotherm parameters calculated from the slopes and intercepts can be seen in Table 5. Langmuir model had the best fitting, suggesting the formation of OTC monolayer on the $PC_{SW/CO2/700/60}$ surface and no further adsorption occurred after the formation of the monolayer, and there was no OTC molecules transmigrated in the plane of the neighboring surface. Moreover, each OTC molecule had similar enthalpy and activation energy [43]. Based on the Langmuir constant, the maximum monolayer adsorption capacity of $PC_{SW/CO2/700/60}$ for OTC was calculated to be 100 mg g^{-1}. Comparison of OTC adsorption capacities of $PC_{SW/CO2/700/60}$ and other absorbents can be seen from Table 6.

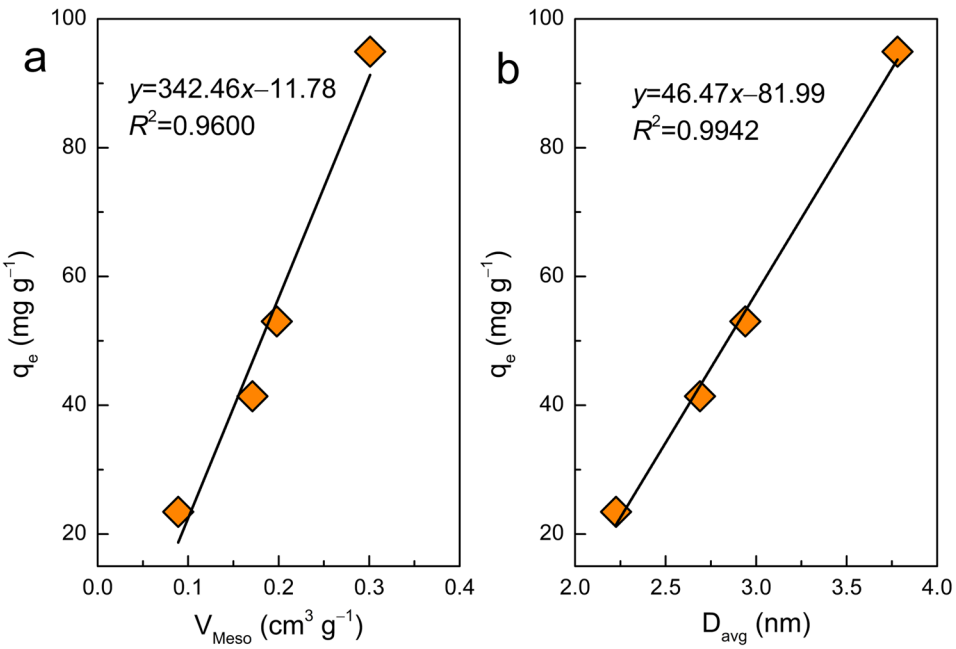

Fig. 11 Linear relationships of q_e with **a** V_{Meso} and **b** D_{Avg}

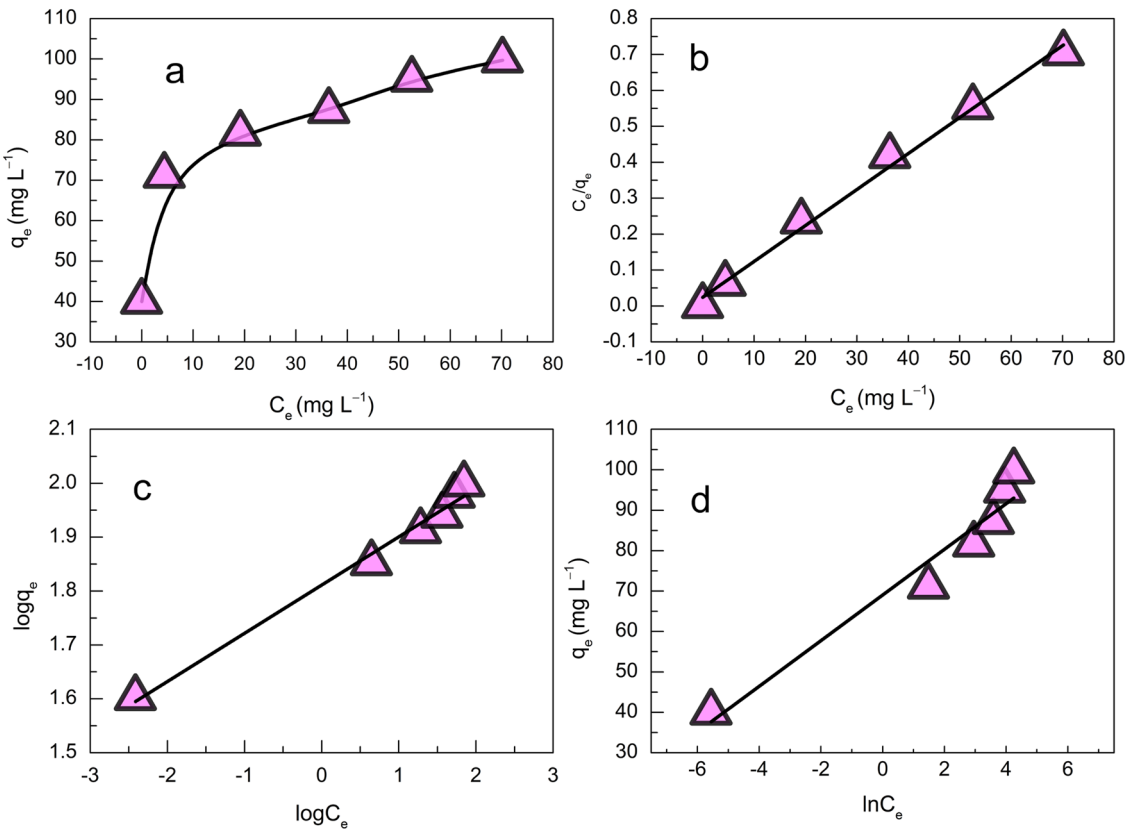

Fig. 12 **a** Adsorption isotherm of OTC on $PC_{SW/CO2/700/60}$, linear fitting of equilibrium isotherm data by **b** Langmuir, **c** Freundlich, and **d** Temkin isotherm models.

Table 5 Fitting parameters for Langmuir, Freundlich and Temkin isotherm model

Langmuir			Freundlich			Temkin		
q_m	K_L	R^2	KF	n	R^2	A_T	B_T	R^2
100	0.30	0.9942	64.72	11.17	0.9847	2.04×10^5	5.65	0.9339

Table 6 Comparison of OTC adsorption capacities of various absorbents

Adsorbent	Adsorption capacity (mg g^{-1})	Refs.
Halloysite nanoclay	22.42	[49]
Magnetic montmorillonite-biochar composite	58.85	[50]
CuMnAl hydroxide	250	[51]
Surfactant-modified-alumina	143	[52]
Multiwalled carbon nanotube	73	[53]
Graphene oxide functionalized magnetic particles	45	[54]
$PC_{SW/CO2/700/60}$	100	This study

4 Conclusion

1. Seawater impregnation benefited the decomposition of sawdust at low temperatures and the formation of char. More CO was produced from seawater impregnated sawdust than from the untreated sawdust under CO_2 at the 700 and 890 °C, indicating a higher degree of activation. 700 °C was selected as the activation temperature for the purpose of energy-saving.
2. Because of seawater impregnation, BET surface area and total pore volume of porous carbon increased from 331 $m^2\ g^{-1}$ and 0.238 $cm^3\ g^{-1}$ to 600 $m^2\ g^{-1}$ and 0.402 $cm^3\ g^{-1}$, respectively, without changing the activation condition. A longer period of activation time led to the formation of remarkably more mesopores.
3. Micro-mesoporous carbon with a BET surface area of 490 $m^2\ g^{-1}$ and an average pore diameter of 3.78 nm can be prepared from seawater impregnated sawdust after 60-min activation. Its adsorption equilibrium data for OTC followed Langmuir model with a maximum monolayer adsorption capacity up to 100 mg g^{-1}.

Acknowledgements The authors wish to thank the editor and the anonymous reviewers for their comments.

Funding This work was funded by National Natural Science Foundation of China (51909292) and Fundamental Research Funds for Central Public Welfare Scientific Research Institution (K-JBYWF-2019-ZT02, K-JBYWF-2017-G19, K-JBYWF-2017-T09).

Compliance with ethical standards

Conflict of interest The authors declare that they have no conflict of interest.

References

1. Yang X-x, Hou X-f, Gao X-m, Fu F (2019) Hierarchical porous carbon from semi-coke via a facile preparation method for p-nitrophenol adsorption. Colloid Surf A 563:50–58
2. Wang J, Sun C, Lin B-C, Huang Q-X, Ma Z-Y, Chi Y, Yan J-H (2018) Micro- and mesoporous-enriched carbon materials prepared from a mixture of petroleum-derived oily sludge and biomass. Fuel Process Technol 171:140–147
3. Enterría M, Suárez-García F, Martínez-Alonso A, Tascón JMD (2012) Synthesis of ordered micro-mesoporous carbons by activation of SBA-15 carbon replicas. Micropor Mesopor Mat 151:390–396
4. Huggins TM, Haeger A, Biffinger JC, Ren ZJ (2016) Granular biochar compared with activated carbon for wastewater treatment and resource recovery. Water Res 94:225–232
5. Xu X, Schierz A, Xu N, Cao X (2016) Comparison of the characteristics and mechanisms of Hg(II) sorption by biochars and activated carbon. J colloid Interface Sci 463:55–60
6. Gottipati R, Mishra S (2016) Preparation of microporous activated carbon from *Aegle Marmelos* fruit shell and its application in removal of chromium(VI) from aqueous phase. J Ind Eng Chem 36:355–363
7. Jia M, Wang F, Jin X, Song Y, Bian Y, Boughner LA, Yang X, Gu C, Jiang X, Zhao Q (2016) Metal ion–oxytetracycline interactions on maize straw biochar pyrolyzed at different temperatures. Chem Eng J 304:934–940
8. Mahamad MN, Zaini MAA, Zakaria ZA (2015) Preparation and characterization of activated carbon from pineapple waste biomass for dye removal. Int Biodeter Biodegr 102:274–280
9. Osuchowski Ł, Szczęśniak B, Choma J, Jaroniec M (2019) High benzene adsorption capacity of micro-mesoporous carbon spheres prepared from XAD-4 resin beads with pores protected effectively by silica. J Mater Sci 54:13892–13900
10. Jeong Y, Cui M, Choi J, Lee Y, Kim J, Son Y, Khim J (2019) Development of modified mesoporous carbon (CMK-3) for improved adsorption of bisphenol-A. Chemosphere 238:124559
11. Nelson KM, Mahurin SM, Mayes RT, Williamson B, Teague CM, Binder AJ, Baggetto L, Veith GM, Dai S (2016) Preparation and CO_2 adsorption properties of soft-templated mesoporous

carbons derived from chestnut tannin precursors. Micropor Mesopor Mat 222:94–103
12. Singh SK, Townsend TG, Mazyck D, Boyer TH (2012) Equilibrium and intra-particle diffusion of stabilized landfill leachate onto micro- and meso-porous activated carbon. Water Res 46:491–499
13. Jain A, Balasubramanian R, Srinivasan MP (2015) Tuning hydrochar properties for enhanced mesopore development in activated carbon by hydrothermal carbonization. Micropor Mesopor Mat 203:178–185
14. Yu L, Luo Y-m (2014) The adsorption mechanism of anionic and cationic dyes by Jerusalem artichoke stalk-based mesoporous activated carbon. J Environ Chem Eng 2:220–229
15. Dehkhoda AM, Gyenge E, Ellis N (2016) A novel method to tailor the porous structure of KOH-activated biochar and its application in capacitive deionization and energy storage. Biomass Bioenerg 87:107–121
16. Angin D, Altintig E, Kose TE (2013) Influence of process parameters on the surface and chemical properties of activated carbon obtained from biochar by chemical activation. Bioresource Technol 148:542–549
17. Apaydın-Varol E, Erülken Y (2015) A study on the porosity development for biomass based carbonaceous materials. J Taiwan Inst Chem E 54:37–44
18. Rashidi NA, Yusup S (2017) A review on recent technological advancement in the activated carbon production from oil palm wastes. Chem Eng J 314:277–290
19. Kılıç M, Apaydın-Varol E, Pütün AE (2012) Preparation and surface characterization of activated carbons from Euphorbia rigida by chemical activation with $ZnCl_2$, K_2CO_3, NaOH and H_3PO_4. Appl Surf Sci 261:247–254
20. Yagmur E, Inal IIG, Gokce Y, Ulusoy Ghobadi TG, Aktar T, Aktas Z (2018) Examination of gas and solid products during the preparation of activated carbon using phosphoric acid. J Environ Manag 228:328–335
21. Baek J, Lee H-M, Roh J-S, Lee H-S, Kang HS, Kim B-J (2016) Studies on preparation and applications of polymeric precursor-based activated hard carbons: I. Activation mechanism and microstructure analyses. Micropor Mesopor Mat 219:258–264
22. Rashidi NA, Yusup S, Ahmad MM, Mohamed NM, Hameed BH (2012) Activated carbon from the renewable agricultural residues using single step physical activation: a preliminary analysis. APCBEE Procedia 3:84–92
23. Taer E, Deraman M, Talib IA, Umar AA, Oyama M, Yunus RM (2010) Physical, electrochemical and supercapacitive properties of activated carbon pellets from pre-carbonized rubber wood sawdust by CO_2 activation. Curr Appl Phys 10:1071–1075
24. Phuriragpitikhon J, Ghimire P, Jaroniec M (2019) Tannin-derived micro-mesoporous carbons prepared by one-step activation with potassium oxalate and CO_2. J Colloid Interface Sci 558:55–67
25. Yang K, Peng J, Xia H, Zhang L, Srinivasakannan C, Guo S (2010) Textural characteristics of activated carbon by single step CO_2 activation from coconut shells. J Taiwan Inst Chem E 41:367–372
26. Gonçalves GdC, Pereira NC, Veit MT (2016) Production of bio-oil and activated carbon from sugarcane bagasse and molasses. Biomass Bioenerg 85:178–186
27. Zhang T, Walawender W, Fan L, Fan M, Daugaard D, Brown R (2004) Preparation of activated carbon from forest and agricultural residues through CO_2 activation. Chem Eng J 105:53–59
28. Pallarés J, González-Cencerrado A, Arauzo I (2018) Production and characterization of activated carbon from barley straw by physical activation with carbon dioxide and steam. Biomass Bioenerg 115:64–73
29. Duan L-q, Ma Q-s, Ma L-j, Dong L, Wang B, Dai X-q, Zhang B (2019) Effect of the CO_2 activation parameters on the pore structure of silicon carbide-derived carbons. New Carbon Mater 34:367–372
30. Lahijani P, Zainal ZA, Mohamed AR, Mohammadi M (2013) CO_2 gasification reactivity of biomass char: catalytic influence of alkali, alkaline earth and transition metal salts. Bioresource Technol 144:288–295
31. Sadhwani N, Adhikari S, Eden MR, Wang Z, Baker R (2016) Southern pines char gasification with CO_2—kinetics and effect of alkali and alkaline earth metals. Fuel Process Technol 150:64–70
32. He Q, Guo Q, Ding L, Wei J, Yu G (2019) CO_2 gasification of char from raw and torrefied biomass: reactivity, kinetics and mechanism analysis. Bioresource Technol 293:122087
33. Liu Y, Guan Y, Zhang K (2018) CO_2 gasification performance and alkali/alkaline earth metals catalytic mechanism of Zhundong coal char. Korean J Chem Eng 35:859–866
34. Perander M, DeMartini N, Brink A, Kramb J, Karlström O, Hemming J, Moilanen A, Konttinen J, Hupa M (2015) Catalytic effect of Ca and K on CO_2 gasification of spruce wood char. Fuel 150:464–472
35. Lv D, Xu M, Liu X, Zhan Z, Li Z, Yao H (2010) Effect of cellulose, lignin, alkali and alkaline earth metallic species on biomass pyrolysis and gasification. Fuel Process Technol 91:903–909
36. Lavtizar V, Kimura D, Asaoka S, Okamura H (2018) The influence of seawater properties on toxicity of copper pyrithione and its degradation product to brine shrimp *Artemia salina*. Ecotox Environ Safe 147:132–138
37. Atzori G, Mancuso S, Masi E (2019) Seawater potential use in soilless culture: a review. Sci Hortic Amsterdam 249:199–207
38. Ma Y, Wang J, Zhang Y (2019) 'Green tide' to biochar: preparation and adsorption isotherms for three typical organic pollutants. Prog React Kinet Mec 43:30–40
39. Lin X, Kong L, Cai H, Zhang Q, Bi D, Yi W (2019) Effects of alkali and alkaline earth metals on the co-pyrolysis of cellulose and high density polyethylene using TGA and Py-GC/MS. Fuel Process Technol 191:71–78
40. Zhang S, Dong Q, Zhang L, Xiong Y (2016) Effects of water washing and torrefaction on the pyrolysis behavior and kinetics of rice husk through TGA and Py-GC/MS. Bioresource Technol 199:352–361
41. Ma Z, Chen D, Gu J, Bao B, Zhang Q (2015) Determination of pyrolysis characteristics and kinetics of palm kernel shell using TGA–FTIR and model-free integral methods. Energ Convers Manag 89:251–259
42. Cao J, Gao Y, Ma Y (2019) Facile preparation of activated carbon foam via pyrolysis of waste bread under CO_2 atmosphere. Biomass Convers Bior 9:521–529
43. Cao J, Ma Y (2019) Direct preparation of activated carbon fiber aerogel via pyrolysis of cotton under CO_2 atmosphere and its adsorption of methylene blue. Energ Source Part A. https://doi.org/10.1080/15567036.2019.1602221
44. Girgis BS, Soliman AM, Fathy NA (2011) Development of micro-mesoporous carbons from several seed hulls under varying conditions of activation. Micropor Mesopor Mat 142:518–525
45. Banna Motejadded Emrooz H, Maleki M, Shokouhimehr M (2019) Excellent adsorption of orange acid II on a water fern–derived micro- and mesoporous carbon. J Taiwan Inst Chem E 102:99–109
46. Marrakchi F, Ahmed MJ, Khanday WA, Asif M, Hameed BH (2017) Mesoporous-activated carbon prepared from chitosan flakes via single-step sodium hydroxide activation for the adsorption of methylene blue. Int J Biol Macromol 98:233–239
47. Huang Y, Li S, Lin H, Chen J (2014) Fabrication and characterization of mesoporous activated carbon from Lemna minor using one-step H_3PO_4 activation for Pb(II) removal. Appl Surf Sci 317:422–431

48. Sobrinho RAL, Andrade GRS, Costa LP, de Souza MJB, de Souza A, Gimenez IF (2019) Ordered micro-mesoporous carbon from palm oil cooking waste via nanocasting in HZSM-5/SBA-15 composite: preparation and adsorption studies. J Hazard Mater 362:53–61
49. Ramanayaka S, Sarkar B, Cooray AT, Ok YS, Vithanage M (2019) Halloysite nanoclay supported adsorptive removal of oxytetracycline antibiotic from aqueous media. J Hazard Mater 384:121301
50. Liang G, Wang Z, Yang X, Qin T, Xie X, Zhao J, Li S (2019) Efficient removal of oxytetracycline from aqueous solution using magnetic montmorillonite-biochar composite prepared by one step pyrolysis. Sci Total Environ 695:133800
51. Eniola JO, Kumar R, Al-Rashdi AA, Barakat MA (2019) Hydrothermal synthesis of structurally variable binary CuAl, MnAl and ternary CuMnAl hydroxides for oxytetracycline antibiotic adsorption. J Environ Chem Eng. https://doi.org/10.1016/j.jece.2019.103535
52. Pham TD, Tran TT, Le VA, Pham TT, Dao TH, Le TS (2019) Adsorption characteristics of molecular oxytetracycline onto alumina particles: the role of surface modification with an anionic surfactant. J Mol Liq 287:110900
53. Oleszczuk P, Xing B (2011) Influence of anionic, cationic and nonionic surfactants on adsorption and desorption of oxytetracycline by ultrasonically treated and non-treated multiwalled carbon nanotubes. Chemosphere 85:1312–1317
54. Lin Y, Xu S, Li J (2013) Fast and highly efficient tetracyclines removal from environmental waters by graphene oxide functionalized magnetic particles. Chem Eng J 225:679–685